Journal of Solid State Chemistry 182 (2009) 2061–2067

Contents lists available at ScienceDirect

Journal of Solid State Chemistry

journal homepage: www.elsevier.com/locate/jssc

Preparation, characterization of the Ta-doped ZnO nanoparticles and their photocatalytic activity under visible-light illumination

Ji-Zhou Kong, Ai-Dong Li *, Hai-Fa Zhai, You-Pin Gong, Hui Li, Di Wu

National Laboratory of Solid State Microstructures, Materials Science and Engineering Department, Nanjing University, Nanjing 210093, PR China

ARTICLE INFO

Article history:
Received 17 March 2009
Accepted 28 March 2009
Available online 8 April 2009

Keywords:
Home-made water-soluble tantalum precursor
Tantalum-doped ZnO nanocrystals
Visible light
Photocatalytic degradation
Methylene blue decomposition

ABSTRACT

This paper describes a novel catalyst of the Ta-doped ZnO nanocrystals prepared by a modified polymerizable complex method using the water-soluble tantalum precursor as the sources of Ta. The catalysts were characterized by means of various analytical techniques as a function of Ta content ($x = 0$–4 mol%) systematically. A remarkable advantage of the results was confirmed that dopant Ta enhanced the visible-light absorption of ZnO and the low-solubility tantalum doping could restrain the growth of crystal and minish the particle size. The relationship between the physicochemical property and the photocatalytic performance was discussed, and it was found that the photocatalytic activity in the photochemical degradation of methylene blue under visible-light irradiation ($\lambda \geqslant 420$ nm) was dependent on the contents of the dopant, which could affect the particle size, concentration of surface hydroxyl groups and active hydrogen-related defect sites, and the visible-light absorption. The highest photocatalytic activity was obtained for the 1.0 mol% Ta-doped ZnO sample.

1. Introduction

In recent years, air and water pollution widely caused by the industries often results in many environmental problems, which have provided the impetus for extended and intensive research in the area of environmental remediation [1–3]. The wide bandgap semiconductor oxides, such as TiO_2 and ZnO, have been proven as the attractive photocatalysts because they are environmentally sustainable with high catalytic efficiency [4–7]. The design and fabrication of nanostructured semiconductor metal oxides with the tunable physical–chemical properties for advanced catalytic applications have drawn a great deal of attention in the modern catalysis field [8–11]. A massive amount of research work on semiconductor based heterostructure (e.g. semiconductor/semiconductor and metal/semiconductor) nanocatalysts have been triggered in recent years because of their excellent catalytic activity [12–15]. Some transition metal ions were used to dope semiconductors to promote interfacial charge-transfer kinetics [16–22]. In addition, it has been largely emphasized in the literature that the relationship between the size dependence and the catalytic efficiency is close-knit [23–26].

ZnO is known to be one of the important photocatalysts because of its many advantages, such as low price, large initial rates of activities, many active sites with high surface reactivity, high absorption efficacy of light radiations, and environmental-safety. But it also has several drawbacks, including the fast recombination rate of the photogenerated electron–hole pair and a low quantum yield in the photocatalytic reactions in aqueous solutions, which obstruct commercialization of the photocatalytic degradation. Enhancement in the optical absorption urges the scientists to further investigate the undoped and doped ZnO NPs and their photocatalytic activities. Some researchers have modified ZnO by doping with Pb ion [27] and Ag ion [28] to enhance photocatalytic efficiency, owing to the increase of surface defects. Unfortunately, ZnO doped with these ions could also result in environmental contaminants at the same time because of the involved heavy metal ions.

Recently, several groups discovered high photocatalytic decomposition of water in some tantalates [29]. Zou et al. firstly reported that the direct splitting of water under visible-light irradiation with an oxide semiconductor photocatalyst of $InTaO_4$ [30]. Kudo and Kato et al. deeply studied the photocatalytic properties of some alkaline and alkaline earth tantalates and niobates including $Sr_2Ta_2O_7$, $Sr_2Nb_2O_7$, and $NaTaO_3$ [29,31]. In summary, tantalum element has been widely utilized in the photocatalysis. Generally speaking, the majority of powder synthesis of these tantalate photocatalysts has been carried out via the conventional solid-state reaction (SSR) route under high temperatures (typically 1000–1300 °C). However, the ubiquitous problems of the SSR route are the growth of crystal, segregation of components, and possible loss of stoichiometry owing to the volatilization of the compositive components at high temperatures. These factors may result in the decrease of the photocatalytic activity. Recently, low-temperature, wet-chemical

* Corresponding author. Fax: +86 25 83595535.
E-mail address: adli@nju.edu.cn (A.D. Li).

0022-4596/$ - see front matter © 2009 Elsevier Inc. All rights reserved.
doi:10.1016/j.jssc.2009.03.022

methods have been employed to prepare the nanosized crystallites with higher purity and uniform sizes. In these synthetical processes, the typical tantalum precursors, e.g. tantalum isopropoxide [32], tantalum ethoxide [33], and tantalum chloride [34] were utilized, but the major drawback of these precursors is either the high cost or the extreme moisture sensitivity. Although a simple polymerizable complex (PC) route has been developed to solve these problems, the air-stable water-soluble tantalum precursors are still not easily available.

In this work, in order to improve the photocatalytic performance of ZnO, the home-made water-soluble tantalum precursor was firstly explored as the source of dopant Ta to modify ZnO. Water-soluble peroxo-citrato-tantalum precursor was synthesized using Ta_2O_5 as a starting Ta source by a facile basic-flux method, and then the nano-sized Ta-doped ZnO powders were prepared through a modified PC method [35,36]. The influence of the Ta contents on the structure, morphology, and photocatalytic activity of the Ta-doped ZnO nanoparticles (NPs) were investigated systematically, and low-solubility dopant Ta could restrain the growth of crystal and minish the particle size. The nanocrystals of 1 mol% Ta-doped ZnO exhibit excellent photocatalytic activity under the visible-light irradiation ($\lambda \geqslant 420$ nm). The possible photocatalytic mechanism for the photodegradation of methylene blue (MB) has also been proposed.

2. Experimental section

2.1. Chemicals and materials

Zinc nitrate ($Zn(NO_3)_2 \cdot 6H_2O$), citric acid (CA), glacial acetic acid (HAc), tantalum oxide (Ta_2O_5), potassium hydroxide (KOH), ethylene glycol (EG), hydrogen peroxide (H_2O_2), acetylacetone, and nitric acid (HNO_3) were purchased from Nanjing Chemical Reagent Co., Ltd. Poly (vinyl pyrrolidone) (PVP, $M_W \approx 100\,000$) and hydroxypropyl cellulose (HPC, $M_W \approx 100\,000$) were purchased from Aldrich. All chemicals were used directly without further purification. Deionized (DI) water was used throughout all the experiments.

2.2. Synthesis of the water-soluble peroxo-citrato-tantalum

Water-soluble tantalum precursor was synthesized using the stable and cheap Ta_2O_5 as a starting source of Ta element by a simple basic-flux method [37]. Ta_2O_5 and KOH were mixed with the molar ratio of K:Ta = 10 and then fused at 400 °C for 4 h in an alumina crucible. The melt was dissolved with DI water when it cooled to room temperature. After filtration, a clear transparent solution was obtained. White precipitates of hydrous tantalum oxide ($Ta_2O_5 \cdot nH_2O$) were formed after an addition of certain HAc with continuous stirring, and collected by centrifuging. These products were washed with diluted HNO_3 solution (pH < 3) and DI water several times to remove the potassium and possible aluminum ions. Then the washed precipitates were dissolved in aqueous solution of citric acid as chelating agents and H_2O_2 was employed to speed up the reaction, with the molar ratio of Ta ions to citric acid to H_2O_2 of 1:2.5:2.5. Finally, the mixture was heated at 60 °C with continuous stirring to form a transparent water-soluble Ta precursor complex, which was the water-soluble peroxo-citrato-tantalum.

2.3. Preparation of Ta-doped ZnO NPs

Ta-doped ZnO powders were prepared through a modified PC method. Zinc nitrate of 2.975 g was dissolved into 50 mL DI water in a 100 mL beaker with CA, which could be used as a complexant in 1:1 molar ratio with respect to the metal nitrate, then stirred for 1 h in the ambient temperature (solution A). Certain water-soluble peroxo-citrato-tantalum was mixed with EG as crossing-linking at the molar ratio of EG to the metal nitrate of 10:1 (solution B). PVP as surfactant with the concentration 2.0×10^{-2} g/mL and HNO_3 used as catalyst in the volume ratio 1:100 with respect to the mixture of the solution A and B were added. The resultant mixture solution was further sonicated for 15 min and then evaporated at 50 °C until it was condensed to a 70% amount of the original weight. HPC and acetylacetone were put into the above solution as the steric dispersant and stabilizer with the concentration 3.5×10^{-3} g/mL and 2.5×10^{-1} mol/L, respectively. A colorless transparent sol was obtained, then aged for 24 h in air at room temperature and subsequently baked at 140 °C for 12 h for polyesterification, the resultant dark gray glassy resin finally underwent a two-step heat treatment to yield the final products: firstly pyrolysis at 400 °C for 2 h and then annealing at 700 °C for 1 h in air atmosphere. ZnO nanocrystals were also prepared by the same procedure without the addition of the water-soluble tantalum solution. The doping concentrations of tantalum are expressed in mol%.

2.4. Characterizations

The thermal-decomposition characteristics were evaluated by thermogravimetry and differential scanning calorimetry (TG-DSC, STA 409 PC, Netzsch) with a heating rate of 5 °C/min under the air flow. The purity of the water-soluble Ta precursor and tantalum content in the materials were estimated by the inductively coupled plasma resonance (ICP, JY-38 S, JY). The structures of the Ta-doped ZnO NPs were characterized by the X-ray diffraction (XRD) equipment (D/max 2000, Rigaku) using Cu $K\alpha$ radiation at $\lambda = 1.5405$ Å. The infrared (IR) and UV–vis diffuse reflectance spectra (DRS) of the samples were recorded by a FT-IR spectrometer (Nexus-870, Thermo Nicolet) and a UV–vis–NIR spectrophotometer (UV-3600, Shimadzu), respectively. The specific surface area (BET) was estimated by the surface area apparatus (TriStar-3000, Micromeritics). The Ta content in Ta-doped ZnO samples was determined by ICP. The morphology and microstructure of the pure ZnO and Ta-doped ZnO NPs were examined by high-resolution transmission electron microscopy (HRTEM, Tecnai G^2 F20, Philips).

2.5. Measurement of photocatalytic activity

For photocatalytic measurement, all experiments were performed in the aqueous solution containing MB under the similar conditions. The photocatalytic reaction system consisted of a Xe arc lamp (300 W, Ushio) located 10 cm away from the reaction solution, a cut-off filter (providing the visible light, $\lambda \geqslant 420$ nm) and a water filter (preventing from thermal catalytic effect, average temperature 25 ± 0.5 °C). 50 mg of each catalyst was put into 50 mL of a standard MB aqueous solution (10 mg/L) in a 100 mL beaker and agitated for 30 min in the absence of light to attain the equilibrium adsorption. After each given irradiation time, about 3.5 mL of the mixture was withdrawn and separated by centrifuging to remove any suspended solids. The degradation process was monitored by a UV–vis–NIR spectrophotometer (UV-3600, Shimadzu; measuring the maximum absorption of MB at 664 nm).

3. Results and discussion

3.1. Water-soluble peroxo-citrato-tantalum

Water-soluble peroxo-citrato-tantalum precursor was synthesized using Ta_2O_5 by a conventional basic-flux method. It exhibits

excellent stability and long shelf life. No precipitation was observed after a year stock in ambient, indicating that the structure of the chelating organic ligands (COO–Ta–O) do not change in the complexes and the water-soluble precursors is comparatively steady. In order to characterize the decomposition behavior of tantalum precursor, water-soluble peroxo-citrato-tantalum precursor solution was baked at 180 °C for 4 h to obtain powdered precursor.

Fig. 1 shows the TG-DSC curves of the powdered precursor with a heating rate of 5 °C/min in air up to 600 °C. There is one exothermic peak with a broad left trail on the DSC curve at 425 °C related to the decomposition and burning of the peroxo-citrato-tantalum complex, accompanied by a dramatic weight loss of 60% from 200 to 450 °C on the TG curve. After 450 °C, the weight basically keeps constant and the decomposition of peroxo-citrato-tantalum precursor is completed. The precursor purity was detected by ICP, whose result indicates that the Ta precursor has higher Ta ion purity over 99.5%, which is in good agreement with the purity of the starting material of Ta_2O_5. Using home-made Ta precursor solution, the photocatalysts have been prepared at lower processing temperature by a modified PC route.

3.2. Ta-doped ZnO NPs

As described in the Experimental section, the dark gray glassy resin products were prepared through a modified PC method. When acetylacetone was finally added to the mixture of solution A and B with stirring, the colorless transparent precursor was formed gradually. The chemical reactions for the formation of the nanopowders could be formulated as follows:

$$\text{citric acid} + \text{metallic cation} \xrightarrow[\text{in water}]{\text{stirring}} \text{metallic citrate} \quad (1)$$

$$\text{metallic citrate} + \text{ethylene glycol} \xrightarrow[\text{in water}]{\text{stirring}} \xrightarrow[\text{polyesterification}]{\text{drying}} \text{polymer} \quad (2)$$

$$\text{polymer} \xrightarrow[\text{pyrolysis}]{400\,^\circ\text{C}} \xrightarrow[\text{anneal}]{700\,^\circ\text{C}} \text{metal oxide} \quad (3)$$

In solution A, citric acid combines with metallic ion to form chelating complex-metallic citrate (Eq. (1)). After the mixture of solutions A and B, metallic citrate reacts with EG to form three-dimensional polymer network (Eq. (2)) after polyesterification. In the process of final heat treatment, the glassy resin decomposes gradually to form uniform amorphous metal oxide solid solution.

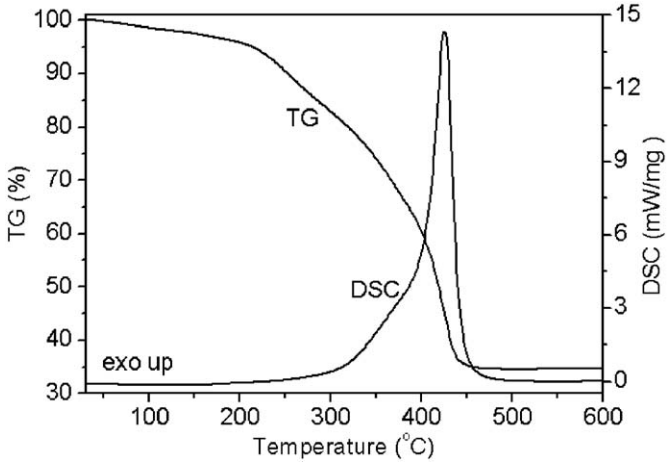

Fig. 1. TG–DSC curves of the peroxo-Ta-citrate powdered precursor heated in air ambience with the heating rate of 5 °C/min.

Subsequently, the crystal nucleation and growth of Ta-doped ZnO happen under high heat-treated temperature (Eq. (3)). Ta^{5+} ions enter into the crystal lattice of ZnO, and may replace the Zn^{2+} ions, leading to the formation of the more zinc vacancy defects (V''_{Zn}) along with some oxygen vacancy defects ($V^{\cdot\cdot}_{O}$) (Eqs. (4) and (5)). Meanwhile due to the high anneal temperature of crystal growth, the loss of oxygen from the lattice can produce oxygen vacancy (Eq. (6)) [38,39]. As known, intrinsic ZnO is a typical n-type semiconductor including large quantities of oxygen vacancies. A lot of experiments have shown that intrinsic defects such as oxygen vacancies are largely involved in the ZnO crystals [40], and can cause high self-compensation via acceptor doping [41]. Similar situation also exists in our Ta-doped ZnO samples.

$$Null = V''_{Zn} + V^{\cdot\cdot}_{O} \quad (4)$$

$$Ta_2O_5 \xrightarrow{ZnO} 2Ta^{\cdot\cdot\cdot}_{Zn} + 3V''_{Zn} + 5O_O \quad (5)$$

$$O_O \rightarrow V^{\cdot\cdot}_{O} + 1/2O_2 + 2e \quad (6)$$

3.2.1. Analysis of phase and morphology of the Ta-doped ZnO NPs

The XRD patterns of pure ZnO and Ta-doped ZnO with different Ta-doping contents annealed at 700 °C are shown in Fig. 2. The XRD patterns of all the Ta-doped ZnO catalysts are almost similar to that of hexagonal wurtzite ZnO, suggesting that there is no change in the crystal structure upon Ta loading. When Ta-doping content is 4 mol%, a weak peak at 30.2° can be indexed to secondary phase of orthorhombic $ZnTa_2O_6$. Remarkably, there is a small shift of all diffraction peaks of ZnO, implying that Ta-doped ZnO solid solution is formed when Ta-doping contents are less than 4%.

The influences of the Ta content ($x = 0$–0.04) on the unit cell parameter (a, c-axis lattice parameter), crystallite size, and specific surface area of Ta-doped ZnO samples are summarized in Table 1. The crystallite size was estimated from the Scherer formula and the specific surface area was measured by means of conventional BET method. The increase of a and c-axis lattice without any change in crystal symmetry indicates that the larger Ta^{5+} ions occupy the Zn^{2+} sites to form Ta-doped ZnO solid solution with the wurtzite structure, which is confirmed by our TEM observations, IR analysis, and UV–visible absorption as described latter. It is easily seen that 1.0 mol% Ta-doped ZnO sample has smallest particle size and largest specific surface area of 32.1 m^2/g. When the Ta content exceeds 1.0 mol%, the particle size increases and specific surface area decreases with the increase of the Ta content. We assume that the low-solubility

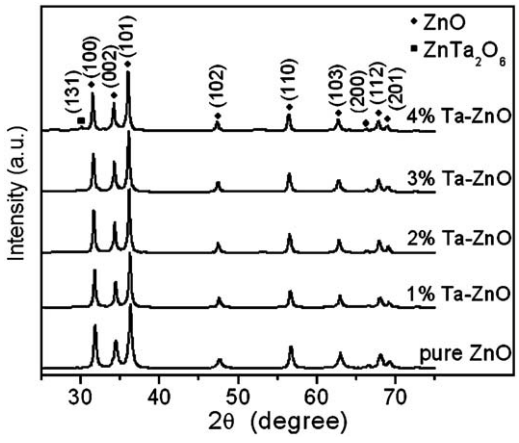

Fig. 2. The XRD patterns of the pure ZnO samples and the Ta-doped ZnO NPs.

Table 1
Particle size, lattice parameter, and specific surface areas of the pure ZnO and Ta-doped ZnO catalysts.

Catalysts	Lattice parameter (Å)		Particle size (nm)	Specific surface area (m^2/g)
	a	*c*		
Pure ZnO	3.2450	5.1995	36.2	22.4
1% Ta–ZnO	3.2464	5.2005	24.8	32.1
2% Ta–ZnO	3.2472	5.2023	29.7	25.8
3% Ta–ZnO	3.2490	5.2041	35.5	21.3
4% Ta–ZnO	3.2499	5.2072	43.3	18.5

Table 2
Analytical result of Ta content in the Ta-doped ZnO catalysts detected by ICP.

Catalysts	Tantalum (%)	
	Nominal	Detected
1% Ta–ZnO	1.0	1.02
2% Ta–ZnO	2.0	2.04
3% Ta–ZnO	3.0	3.06
4% Ta–ZnO	4.0	4.03

dopant could restrain the growth of crystal and minish the particle size [42].

The elemental tantalum content in Ta-doped ZnO samples was analyzed using ICP, as presented in Table 2. The ICP results reveal that the Ta content in Ta-doped ZnO samples is in good agreement with the nominal values. This implies the Ta element from water-soluble peroxo-citrato-tantalum precursor is effectively involved in Ta-doped ZnO samples.

In order to examine the microstructures and morphologies of the samples, TEM observation was carried out. Fig. 3 shows the representative TEM images of the samples with and without the dopant Ta. The pure ZnO sample contains the ZnO nanorods accompanied with the ZnO NPs (Fig. 3a). But after the Ta doping, the nanorods disappear and only the NPs with the spheroidal shape exist (Fig. 3b). When the Ta-doped content is equal to 1.0 mol%, the sizes of the Ta-doped ZnO nanocrystals become much smaller compared with that of the pure ZnO. However, when Ta-doping content exceeds 1.0–4.0%, the sizes of the nanopowder samples gradually increase in good accordance with XRD results. Fig. 3c shows the size distribution of 1% Ta-doped ZnO samples from the statistics of TEM image. It is obvious that the diameters of the nanocrystals are in the range of 22–27 nm with the average diameter of ~25 nm. A typical HRTEM image of 1% Ta-doped ZnO NPs (Fig. 3d) shows the messy and disorder regions in the surface layer. Moreover, some dislocations can be observed, as indicated in the inset taken from the squared area in Fig. 3d. Therefore, we can deduce that there exist more defects on the surface of the nanocrystals prepared by a modified "PC" method.

3.2.2. *Surface structure and optical properties of the Ta-doped ZnO NPs*

The FT-IR spectra for the samples were obtained at the room temperature, as shown in Fig. 4. A few distinct bands are observed in the high wavenumber region, at 3445, 2340, 1640, and 1385 cm^{-1}. Two peaks at 3445 and 1640 cm^{-1} imply that the basic hydroxyl groups of chemisorbed and/or physisorbed H_2O molecules exist in all samples with the hydroxylated surfaces. The one at 2340 cm^{-1} is assigned to the stretching vibration mode of strong Ta=O bands [43]. Another IR peak at 1385 cm^{-1} results from OH^- absorption of hydrogen-related defects [44,45]. Compared with the pure ZnO, the intensity of the peaks at

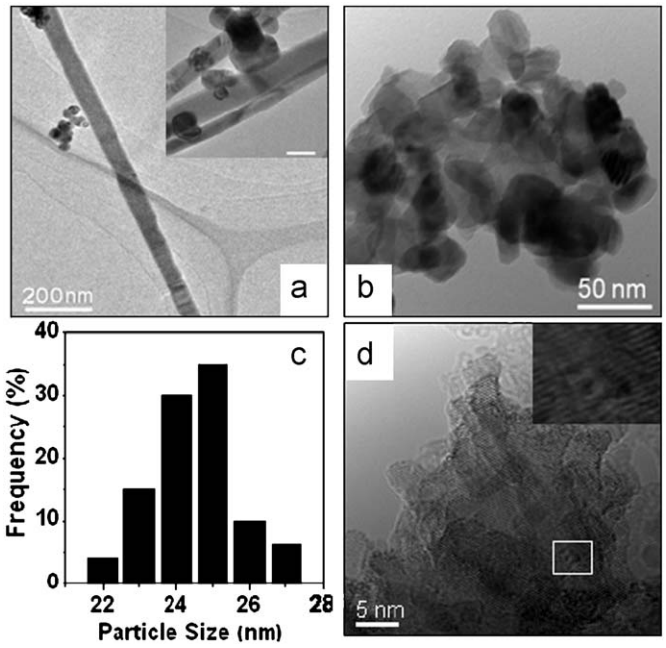

Fig. 3. TEM images of the ZnO samples with and without dopant Ta: (a) the image of pure ZnO, the horizontal bar scale of the inset image is 50 nm; (b) the image of 1% Ta–ZnO; (c) size distribution of 1% Ta–ZnO NPs; and (d) HRTEM image of 1% Ta–ZnO (the inset of the squared region of d).

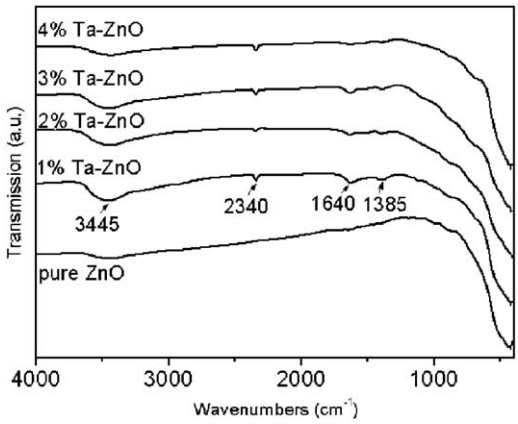

Fig. 4. The FT-IR spectra of the pure ZnO and the Ta-doped ZnO NPs.

3445, 1640, and 1385 cm^{-1} is enhanced when the Ta-doping content gets to 1.0 mol%. But when the Ta-doping content exceeds 1.0 mol%, the intensity of IR peaks at 3445, 1640, and 1385 cm^{-1} becomes weaker step by step. It indicates that the concentration of surface hydroxyl groups and active hydrogen-related defects of samples is related to the Ta-doping content, which affects the photocatalytic activity. This work will be shown in the following part. In addition, a strong absorption band corresponding to the stretching and vibrational modes of metal–oxygen bands (Zn–O/Zn–O–Ta) is also observed for each sample below 1000 cm^{-1}.

The room-temperature UV–visible absorption spectra of the prepared samples were also measured, as shown in Fig. 5. A pressed $BaSO_4$ powder was used as a reference, and the data are plotted as the remission function $F(R) = (1-R)^2/(2R)$, where R is diffuse reflectance based on the Kubelka–Monk theory of diffuse reflectance. It can be seen that there exists a strong absorption edge below 420 nm for all samples. With increasing the Ta-doping content, the absorption edge moves towards the low wavelength

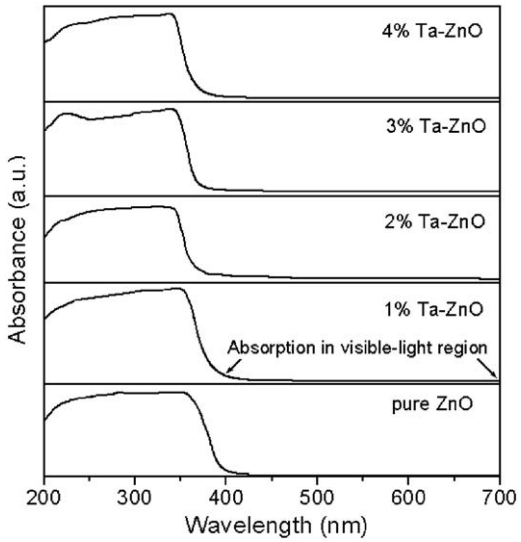

Fig. 5. UV–visible absorption spectra of the undoped and doped ZnO NPs.

and the bandgap becomes large gradually. This demonstrates that Ta^{5+} ions have entered into the lattice of ZnO, in consistent with the XRD results. Another significant and observable change locates the enhanced absorption in the visible-light region ranged from 400 to 700 nm for the Ta-doped ZnO (indicated by arrows), compared with the pure ZnO. This implies that the doping Ta^{5+} ions in ZnO lattices generate more active defect sites below energy level of the conduction band, and thus more visible-light is absorbed via these active defect sites, which is very important for visible-light photodegradation.

For the direct bandgap semiconductor, the relation between the absorption edge and the photon energy ($h\nu$) can be written as follows:

$$(\alpha h\nu)^2 = A(h\nu - E_g) \quad (7)$$

where A is absorption constants decided by the materials of direct bandgap semiconductor. The absorption coefficient (α) is determined from the scattering and reflectance spectra according to Kubelka–Munk theory. The onsets of absorption and direct bandgap energies estimated from the intercept of the tangents to the plots are presented in Table 3. The absorption onsets decrease and the corresponding bandgap values increase with increasing Ta dopant content.

3.2.3. *Photocatalysis and photocatalytic mechanism of the Ta-doped ZnO NPs*

To understand the relationship between the Ta-doping contents and the photocatalytic property, the photocatalytic activity of the annealed samples has been investigated under visible-light irradiation ($\lambda \geqslant 420$ nm). MB was adopted as a representative organic dye to evaluate the photocatalytic performance. In Fig. 6, C_0 is the initial concentration of MB after the equilibrium adsorption, and C_t is the equilibrium concentration of MB at visible-light irradiation time.

As shown in Fig. 6, the degradation of MB without photocatalysts is negligible under visible-light illumination, and the Ta-doped ZnO catalysts exhibit higher photocatalytic activity, compared with that of pure ZnO. The degradation rate of MB catalyzed by Ta-doped ZnO improves with increasing Ta loading, and the Ta-doped ZnO catalysts with 1.0 mol% Ta-doping content show the highest photodegradation rate. While the Ta-doping content (x) exceeds 1.0 mol%, the photocatalytic activity of the Ta-doped ZnO samples decreases with an increase of the Ta-doping content. The photocatalytic efficiency of these catalysts is ranked in an order from the highest to the lowest: 1.0% Ta–ZnO > 1.5% Ta–ZnO > 0.5% Ta–ZnO > 2.0% Ta–ZnO > 3.0% Ta–ZnO > pure ZnO.

In addition, the photocatalytic stability of 1.0 mol% Ta-doped ZnO catalysts was also evaluated. After the photocatalyst has been stored for one month and a half in air, the photocatalytic measurement was performed and lasted for 50 min. Before testing, the sample was dried at 120 °C for 1 h. After photocatalysis, the degradation rate reduced to 94%, almost the same value as that presented in Fig. 6, which verifies the excellent photocatalytic stability of the 1% Ta-doped ZnO photocatalyst because of its high crystallinity.

In order to illuminate the effect of the defects in photocatalysis, the proposed band structure and photocatalytic mechanism for the photodegradation of MB is illustrated in Fig. 7. The defects on the surface of the catalysts promoted in the presence of the Ta dopant are responsible for the photogenerated electron–hole pairs under visible-light irradiation. Activation energy could be ascribed to the oxygen vacancy, which is a deep donor in the catalyst at ~1.0 eV below the bottom of the conduction band, and the lever of the zinc vacancy defect is relatively shallow at approximately 0.4 eV above the top of the valence band [40].

Table 3
UV–vis absorption data for the undoped and doped ZnO nanocatalysts.

Catalysts	λ (nm)	Bandgap (eV)
Pure ZnO	390	3.19
1% Ta–ZnO	385	3.24
2% Ta–ZnO	380	3.28
3% Ta–ZnO	377	3.30
4% Ta–ZnO	368	3.34

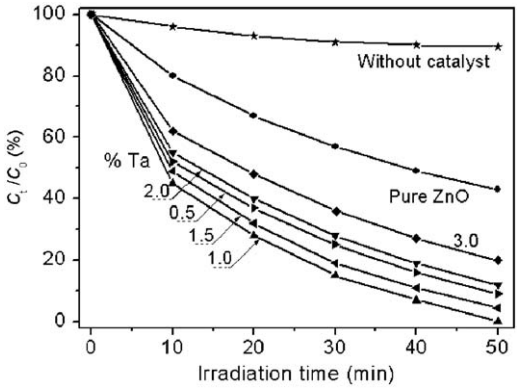

Fig. 6. Photodegradation of MB with respect to the irradiation time using the undoped and doped ZnO NPs exposed to the visible light.

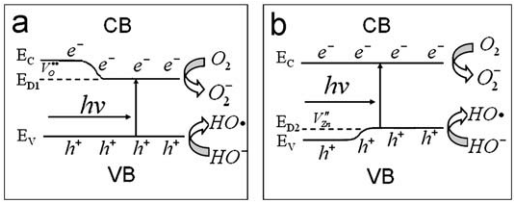

Fig. 7. Proposed band structure and photocatalytic mechanism of the Ta-doped ZnO with the different defects: (a) oxygen vacancy and (b) zinc vacancy, where E_C, E_V, and E_D mean the conduction band, valence band, and intermediate band, respectively.

When the photocatalysts are dispersed in the electrolyte, under the influence of the electric field, the conduction-bands and valence-bands bend. Thus, the migration of the photo-induced electrons and holes toward different kinds of the defects is reasonable [46]. The excited electrons can easily move to the oxygen vacancies on the surface of the catalyst, as presented in Fig. 7a. However, only a few holes could break through a potential barrier to get to the intermediate band E_{D2} from the valence band, as shown in Fig. 7b. Thus, the separation efficiency of the electron–hole pairs of the active oxygen vacancies should be much higher than that of the zinc vacancies.

Under visible-light irradiation, an electron–hole pair forms, and then a conduction-band electron and a valence-band hole separate on the surface of catalyst. Maybe the hole permits the direct oxidation of organic dye to reactive intermediates. Due to the existence of the intermediate state E_D, electrons in the valence band can be excited to the conduction band under visible-light irradiation. In the presence of the dissolved O_2, electrons from the photoexcited Ta-doped ZnO produce superoxide anion radicals O_2^-, which subsequently could generate H_2O_2 and $HO^{\cdot}$ radicals [1,2]. The high oxidative potential of the holes can form very reactive hydroxyl groups through decomposing of water. The active oxygen vacancies severed as electron acceptors can trap the photo-induced electrons temporarily to restrain the surface recombination of photogenerated electrons and holes, and then attack the dissolved O_2 to yield surface-bound superoxide anion radicals O_2^- or hydroxy groups, which can act as effective centers of organic matter mineralization for photocatalytic reactions [11].

On the basis of the above experimental results and discussion, it is concluded in photocatalysis of Ta-doped ZnO as follows: (1) Ta-doped ZnO powders serve as electron and hole sources for degradation of organic dye. The doped Ta^{5+} ions in the crystal of ZnO play an important role in coming into being the hole–electron pairs. (2) The defects, including oxygen defects, hydrogen-related defects, and so forth, benefit the efficient separation of the electron–hole pairs and minimize the recombination reactions of chemical products. With increasing Ta-doping content over 1 mol%, the active and valid defects for photodegradation decrease, as confirmed above. (3) Surface hydroxy groups also act as the effective centers of organic matter mineralization in the photocatalysis. The more surface hydroxy groups lead to the higher photocatalytic efficiency.

By far, as we have known, the homogeneous substitution of Zn^{2+} in the lattice of ZnO by Ta^{5+} can cause a series of changes in the structural, morphological, optical, and photocatalytic properties, such as the lattice parameter, bandgap, grain size, active defect sites, and visible-light absorption. Our experiments have shown that 1 mol% Ta-doped ZnO nanocatalyst exhibit excellent photodegradation activity. Based on the results of the IR, XRD, and specific surface area, the 1 mol% Ta-doped ZnO NPs have shown the highest concentration of surface hydroxyl groups and active defects, smallest crystalline size, and largest specific surface area. So it is reasonable for 1 mol% Ta-doped ZnO to achieve the optimal photocatalytic performance in our system.

4. Conclusions

In summary, we have firstly prepared the Ta-doped ZnO samples with different Ta-doping contents through a modified PC method, using the water-soluble peroxo-citrato-tantalum precursor as the source of Ta. A systematic study of the structural, morphological, optical, and visible-light photocatalytic properties of Ta-doped ZnO and pure ZnO samples has been carried out by means of various analytical techniques. It is found that the addition of the dopant Ta not only increases the lattice constants and bandgap of the nanocrystals but also significantly improves the photocatalytic activity under visible-light irradiation. Meanwhile the Ta doping also changes the morphology, surface adsorption, specific surface area, crystalline size, and thus affects the photocatalytic activity. The relationship between the physicochemic properties and the photocatalytic performance of the catalysts is discussed. The related mechanism has been proposed based on our experimental results. Photocatalytic efficiency of the Ta-doped ZnO NPs is much more excellent than the pure ZnO, which is attributed to the increase of the active hydrogen-related defect sites caused by Ta^{5+} doping, leading to the enhanced specific surface area and optical absorption in the visible-light region. The Ta-doping content has been tuned to obtain the optimal photocatalytic property, and the 1.0 mol% Ta-doped ZnO photocatalyst has highest photocatalytic activity owing to the highest concentration of surface hydroxyl groups and active hydrogen-related defect sites, largest specific surface area. Our work demonstrates that the water-soluble Ta precursors from Ta_2O_5 are potential and competitive candidates for the photocatalytic applications, the photocatalysts can be prepared using the precursor as the source of Ta under low-temperature heat treatment. And the Ta-doped ZnO is a promising visible-light photocatalyst for applications in photo-decomposing water contamination and environmental pollution.

Acknowledgments

This project was supported by the Natural Science Foundation of China and Jiangsu Province (50672036, 10704035, and BK2006122) and a grant from the State Key Program for Basic Research of China (2006CB921805, 2009ZX02101-4, and 2009CB929500). We thank the support from the program for the "333" Talents in Jiangsu Province and SRF for ROCS, SEM.

References

[1] V. Kandavelu, H. Kastien, K.R. Thampi, Appl. Catal. B Environ. 48 (2004) 101.
[2] E. Evgenidou, K. Fytianos, I. Poulios, Appl. Catal. B Environ. 59 (2005) 81.
[3] C. Chen, J.L. Wang, J. Hazard. Mater. 151 (2008) 65.
[4] G.H. Li, N.M. Dimitrijevic, L. Chen, J.M. Nichols, T. Rajh, K.A. Gray, J. Am. Chem. Soc. 130 (2008) 5402.
[5] A.A. Presto, E. Granite, J. Environ. Sci. Technol. 40 (2006) 5601.
[6] A. Iglesias-Juez, A. Martinez-Arias, M. Fernandez-Garcia, J. Catal. 221 (2004) 148.
[7] K. Shimizu, H. Kawabata, A. Satsuma, T. Hattori, J. Phys. Chem. B 103 (1999) 5240.
[8] Y.H. Zheng, L. Zheng, Y.Y. Zhan, X.Y. Lin, Q. Zheng, K. Wei, Inorg. Chem. 46 (2007) 6980.
[9] G. Colon, M.C. Hidalgo, J.A. Navio, E.P. Melian, O.G. Diaz, J.M. Dona, Appl. Catal. B Environ. 78 (2008) 176.
[10] H.G. Kim, P.H. Borse, W. Choi, J.S. Lee, Angew. Chem. Int. Ed. 44 (2005) 4585.
[11] G. Marci, V. Augugliaro, M.J. Lopez-Munoz, C. Martin, L. Palmisano, V. Rives, M. Schiavello, R.J.D. Tilley, A.M. Venezia, J. Phys. Chem. B 105 (2001) 1026; G. Marci, V. Augugliaro, M.J. Lopez-Munoz, C. Martin, L. Palmisano, V. Rives, M. Schiavello, R.J.D. Tilley, A.M. Venezia, J. Phys. Chem. B 105 (2001) 1033.
[12] H.Q. Liu, J.X. Yang, J.H. Liang, Y.X. Huang, C.Y. Tangz, J. Am. Chem. Soc. 91 (2008) 1287.
[13] L.N. Lewis, Chem. Rev. 93 (1993) 2693.
[14] F. Zhang, R. Jin, J. Chen, C. Shao, W. Gao, L. Li, N. Guan, J. Catal. 232 (2005) 424.
[15] J.J. Wu, C.H. Tseng, Appl. Catal. B Environ. 66 (2006) 51.
[16] P. Mahata, G. Madras, S. Natarajan, J. Phys. Chem. B 110 (2006) 13759; X.Q. Qiu, G.S. Li, X.F. Sun, L.P. Li, X.Z. Fu, Nanotechnology 19 (2008) 215703.
[17] R. Ullah, J. Dutta, J. Hazard. Mater. 156 (2008) 194.
[18] R. Narayanan, M.A. El-Sayed, J. Am. Chem. Soc. 125 (2003) 8340.
[19] C. Ye, Y. Bando, G. Shen, D. Golberg, J. Phys. Chem. B 110 (2006) 15146.
[20] S. Anandan, A. Vinu, K.L.P.S. Lovely, N. Gokulakrishnan, P. Srinivasu, T. Mori, V. Murugesan, V. Sivamurugan, K. Ariga, J. Mol. Catal. A Chem. 266 (2007) 149.
[21] D. Li, H. Haneda, J. Photochem. Photobiol. A Chem. 160 (2003) 203.
[22] F. Lu, W.P. Cai, Y.G. Zhang, Adv. Funct. Mater. 18 (2008) 1047.
[23] S.J. Li, Z.C. Ma, J. Zhang, J.Z. Liu, Catal. Commun. 9 (2008) 1482.
[24] Q. Zhang, W. Fan, L. Gao, Appl. Catal. B Environ. 76 (2007) 168.
[25] L.Q. Jing, B.F. Xin, F.L. Yuan, L.P. Xue, B.Q. Wang, H.G. Fu, J. Phys. Chem. B 110 (2006) 17860.

[26] N. Pradhan, A. Pal, T. Pal, Langmuir 17 (2001) 1800.
[27] K. Vanhesuden, W.L. Warren, J.A. Voigt, C.H. Seager, D.R. Tallant, Appl. Phys. Lett. 67 (1995) 1280.
[28] R. Wang, J.H. Xin, Y. Yang, H. Liu, L. Xu, J. Hu, Appl. Surf. Sci. 227 (2004) 312.
[29] H. Kato, A. Kudo, J. Phys. Chem. B 105 (2001) 4285.
[30] Z.G. Zou, J.H. Ye, K. Sayama, H. Arakawa, Nature 414 (2001) 625.
[31] A. Kudo, H. Kato, S. Nakagawa, J. Phys. Chem. B 104 (2000) 571.
[32] C.Y. Yue, L.H. Qiu, M. Trudeau, D. Antonelli, Inorg. Chem. 46 (2007) 5084.
[33] N. Ndiege, T. Wilhoite, V. Subramanian, M.A. Shannon, R.I. Masel, Chem. Mater. 19 (2007) 3155.
[34] J.N. Kondo, M. Uchida, K. Nakajima, L. Daling, M. Hara, K. Domen, Chem. Mater. 16 (2004) 4304.
[35] Y. Yamashita, K. Yoshida, M. Kakihana, S. Uchida, T. Sato, Chem. Mater. 11 (1999) 61.
[36] I. Pribosic, D. Makovec, M. Drofenik, Chem. Mater. 17 (2005) 2953.
[37] A.D. Li, J.B. Cheng, R.L. Tang, Q.Y. Shao, Y.F. Tang, D. Wu, N.B. Ming, Mater. Res. Soc. Symp. Proc. 942 (2006) W03–W04.
[38] R. Moos, K.H. Hardtl, J. Appl. Phys. 80 (1996) 393.
[39] J. Yin, J.H. Ye, Z.G. Zou, Appl. Phys. Lett. 85 (2004) 689.
[40] A. Janotti, C.G. Van de Walle, Appl. Phys. Lett. 87 (2005) 122102; A. Janotti, C.G. Van de Walle, J. Cryst. Growth 287 (2006) 58.
[41] Q.X. Wan, Z.H. Xiong, J.N. Dai, J.P. Rao, F.Y. Jiang, Opt. Mater. 30 (2008) 817.
[42] J.J. Zou, B. Zhu, L. Wang, X.W. Zhang, Z.T. Mi, J. Mol. Catal. A 286 (2008) 63.
[43] H. Ono, K. Koyanagi, Appl. Phys. Lett. 77 (2000) 1431.
[44] Z.S. Li, T. Yu, Z.G. Zou, J.H. Ye, Appl. Phys. Lett. 88 (2006) 071917.
[45] J. Lin, J. Lin, Y.F. Zhu, Inorg. Chem. 46 (2007) 8372.
[46] Y.H. Zheng, C.Q. Chen, Y.Y. Zhan, X.Y. Lin, Q. Zheng, K. Wei, J.F. Zhu, Y.J. Zhu, Inorg. Chem. 46 (2007) 6675.